Electron transport across carbon nanotube junctions decorated with Au nanoparticles: Density functional calculations

K. H. Khoo[1] and James R. Chelikowsky[1,2]

[1]*Center for Computational Materials, Institute of Computational Engineering and Sciences, University of Texas at Austin, Austin, Texas 78712, USA*

[2]*Department of Physics and Department of Chemical Engineering, University of Texas at Austin, Austin, Texas 78712, USA*

(Received 29 January 2009; revised manuscript received 30 April 2009; published 22 May 2009)

In recent years, there has been extensive research on carbon nanotube networks owing to their potential for applications in transparent electronics. Several experimental studies have found that electrical conductivity across these networks can be increased by metal nanoparticle doping. To aid in understanding the mechanism of this conductance increase, we have performed first-principles calculations on nanotube junctions decorated with small Au nanoparticles. Our calculations show that the conductance of nanotube junctions is increased by the introduction of odd-numbered Au nanoparticles and electron transport is mediated by resonant tunneling through Au nanoparticle states. In addition, we find interesting interference effects that modulate conduction across doped nanotube junctions that connect near nanotube tips.

DOI: 10.1103/PhysRevB.79.205422 PACS number(s): 73.63.Fg, 73.22.−f

I. INTRODUCTION

An area of intense research over the past few years is the chemical modification of carbon nanotubes by decoration with nanoparticles.[1] These hybrid materials have been utilized in a variety of applications such as chemical sensing,[2,3] hydrogen storage,[4,5] catalysis,[6] and nanoscale electronic devices.[7] More recently, this method of nanotube modification has been extended to the functionalization of nanotube thin films.[8–10] Free-standing, transparent, and conductive films of nanotube networks have been fabricated with reproducible device characteristics.[11–13] It has been shown experimentally that the electrical conductivity of these films can be increased by doping with metal nanoparticles,[8] making them excellent materials for transparent electronics applications.

Despite recent advances made in the doping of nanotube networks, there are relatively few theoretical studies focused on such systems. To address this issue, we have performed first-principles calculations to investigate electron transport across Au-nanoparticle-decorated nanotube junctions. This serves as an intermediate step to understanding electrical conduction across doped nanotube networks. From our calculations, it was found that electron transport across these junctions is mediated by Au nanoparticle resonances and the transmission amplitude is strongly dependent on the coupling strength between nanoparticle resonances and nanotube states at the resonance energy. We find that only odd-numbered Au nanoparticles transmit electrons at low bias, owing to the fact that even-numbered Au nanoparticles have a highest occupied molecular orbital–lowest unoccupied molecular orbital (HOMO-LUMO) gap originating from its closed-shell electronic configuration. In addition, an interesting interference effect was found to modulate electron transport across nanotube junctions located near nanotube tips.

II. METHODOLOGY

All calculations performed in this work are based on density functional theory (DFT) utilizing the SIESTA package.[14] A double-ζ pseudoatomic basis set is employed for both Au and C atoms and the cutoff radii of basis orbitals are determined by fixing the energy shift of atomic eigenvalues to 0.01 Ry.[15] Exchange correlation is evaluated using the generalized gradient approximation (GGA) (Ref. 16) and sampling of the real-space grid is controlled with an energy cutoff of 200 Ry. Electron-ion core interactions are represented by norm-conserving pseudopotentials, with scalar-relativistic effects included for Au pseudopotentials.[17]

In order to evaluate the transmission spectra and *I-V* characteristics of nanotube junctions, calculations have been performed employing the scattering-state formalism as outlined elsewhere.[18] In these calculations, the system is partitioned into three regions: the left lead, a finite central resistive region, and the right lead. The Hamiltonian matrices for the semi-infinite left and right leads are obtained from standard first-principles calculations on bulk periodic systems. For calculations at finite bias, the two leads are fixed at different chemical potentials and a solution of the Laplace equation is added to the periodic solution of the Poisson equation of the resistive region. Once the Hamiltonian is obtained, energy-dependent scattering states are constructed on a fine energy grid around the Fermi energy, with incoming and outgoing itinerant and evanescent states determined from the bulk lead complex band structure;[18,19] typical energy grid spacings used in this work are 5 meV. This results in a linear system of equations at each energy E, which are then solved to yield transmission matrix t with elements $t_{nm}(E)$ for each incoming channel n and outgoing channel m. The steady-state charge density $\rho(r)$ can be obtained by integrating contributions from scattering states between the lead chemical potentials, assuming a Fermi-Dirac distribution occupancy specified by the incident lead chemical potential and contributions from stationary eigenstates below the lower lead chemical potential. The resulting $\rho(r)$ is then used to generate a new Hamiltonian and corresponding density following the method outlined above; this process is repeated until self-consistency in $\rho(r)$ is reached. Upon reaching self-consistency, the current is calculated using a Landauer-type formula by integrating

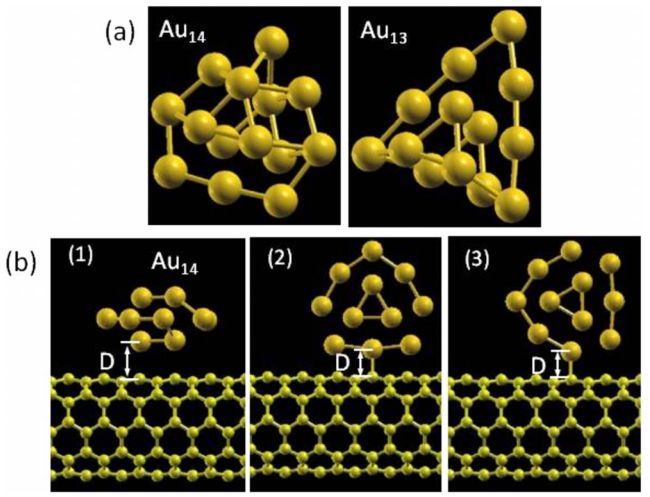

FIG. 1. (Color online) (a) Low-energy Au_{13} and Au_{14} structures. (b) Adsorption orientations of an Au_{14} nanoparticle on a (5,5) single-walled carbon nanotube.

the transmission spectrum (the square of the transmission coefficients) between the two chemical potentials.[18,20] To map out an *I-V* characteristic, the entire procedure is repeated for different bias voltages.

III. RESULTS AND DISCUSSION

The nanotube junctions studied in this work consists of a pair of parallel (5,5) single-walled carbon nanotubes (SWNT) bridged by Au_{13} or Au_{14} nanoparticles. The Au_{13} and Au_{14} geometries are obtained from previous DFT calculations and possess C_{2v} symmetry, as shown in Fig. 1(a).[21] These structures exhibit strong anisotropy due to relativistic effects that enhance directional bonding between Au atoms.[22] We also expect qualitatively different properties from Au_{13}- and Au_{14}-decorated nanotube junctions, as Au nanoparticles are known to exhibit strong even-odd oscillations in their stability and electronic structure.[21,23]

To construct our calculation geometry, we start by identifying low-energy adsorption orientations for Au_{13} and Au_{14} on a (5,5) SWNT. This is done by first relaxing the coordinates of Au nanoparticles and carbon nanotubes separately with a force tolerance of 0.01 eV/Å. Each nanoparticle is then positioned on the nanotube in three test orientations as shown for Au_{14} in Fig. 1(b), and total-energy DFT calculations are performed for each of these geometries inside a supercell. The supercell dimension along the nanotube axis is 6 nanotube unit-cell lengths with a three *k*-point sampling and sufficient vacuum is included in directions perpendicular to the nanotube axis to isolate the system from its periodic images. The total energy is evaluated over a range of nanoparticle-nanotube distances *D* and results for the Au_{14} calculation are plotted in Fig. 2(a). Only non-spin-polarized calculations are discussed in this paper as the inclusion of spin was found to produce negligible changes in the electronic structure of nanotube junctions being studied.

The lowest energy orientation for Au nanoparticle adsorption is determined by two opposing factors. For orientations

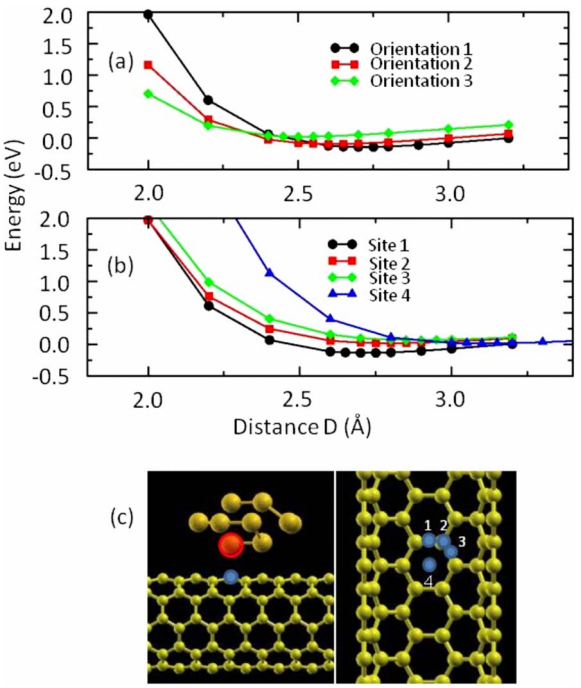

FIG. 2. (Color online) Plots of total energy vs Au_{14}-nanotube distance *D* for (a) Au_{14} adsorption orientations illustrated in Fig. 1(b) and (b) Au_{14} in low-energy orientation centered on sites illustrated in (c). (c) High-symmetry adsorption sites of Au_{14} over (5,5) SWNT.

where a nanoparticle edge adsorbs on the nanotube surface, there are fewer atoms in contact with the nanotube but each atom binds more strongly owing to their lower coordination number. For orientations where a nanoparticle face rests on the nanotube surface, the contact area is maximized at the expense of the binding energy per atom.[24] From the results shown in Fig. 2(a), we see that orientations that maximize the contact area are favored for Au_{14}, with orientation 1 being the lowest in energy and orientation 3 the highest. Corresponding calculations have revealed similar trends for the adsorption of Au_{13} on a (5,5) SWNT.

After determining the low-energy orientations, we proceed to test various Au nanoparticle adsorption positions on the nanotube. The base atom of the Au nanoparticle closest to the nanoparticle center is placed above high-symmetry points picked out on the SWNT, as shown in Fig. 2(c). The total energy is then calculated as a function of the nanoparticle-nanotube distance *D* for both Au_{13} and Au_{14} employing supercell calculations similar to those described previously, with results for Au_{14} plotted in Fig. 2(b). It was found that the lowest energy adsorption position has the selected Au nanoparticle base atom positioned directly above a C-C bond perpendicular to the nanotube axis and the equilibrium nanoparticle-nanotube distances are 2.55 Å and 2.70 Å for Au_{13} and Au_{14}, respectively. At this point, it is also convenient to introduce the coordinate system that will be in use throughout the paper. Let the nanotube axis be the *z* axis and the line perpendicular to the nanotube axis that connects it to the Au nanoparticle center be the *y* axis. Using the geometries obtained above for Au_{13} and Au_{14} nanoparticles adsorbed on a single (5,5) SWNT, we construct the

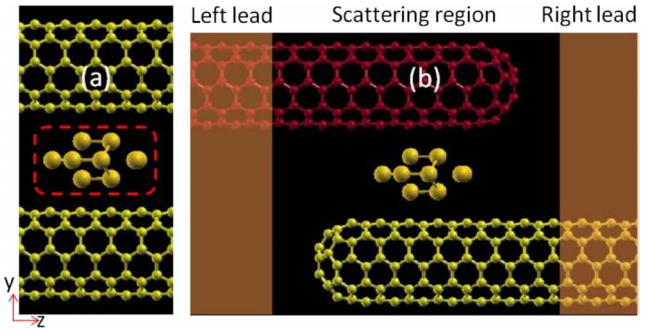

FIG. 3. (Color online) Model geometries for (a) supercell and (b) scattering-state calculations on Au_{14}-decorated carbon nanotube junctions. Shaded areas in (b) denote left and right nanotube lead regions.

corresponding nanotube junctions by introducing an additional nanotube so that the system is symmetric about the xz plane centered on the nanoparticle, as illustrated in Fig. 3(a).

Supercell calculations similar to those discussed previously were then performed and the Au nanoparticle coordinates were relaxed with a force tolerance of 0.01 eV/Å, while keeping the nanotube coordinates fixed. The Au atoms undergo an average atomic displacement of 0.15 Å in Au_{13} and 0.03 Å in Au_{14} upon relaxation and the nanoparticle-nanotube binding energies were calculated to be 2.05 eV for Au_{13} and 1.24 eV for Au_{14}. The larger atomic displacement and binding energy of Au_{13} in the nanotube junction is a consequence of its higher reactivity relative to Au_{14}.[21,23] It was also found from a Mulliken analysis that 0.20 electrons were transferred from both Au_{13} and Au_{14} to the nanotubes in the junction.

To gain more insight into the Au nanoparticle-nanotube interaction in these nanotube junctions, we calculate the density of states projected on isolated Au nanoparticle eigenstates (PDOS) given by $D_i(E)=\Sigma_{nk}\delta(E-E_{nk})|\langle\varphi_i|\psi_{nk}\rangle|^2$, where $|\varphi_i\rangle$ is the ith eigenstate of an isolated Au nanoparticle, $|\psi_{nk}\rangle$ the junction wave function, and E_{nk} the junction eigenenergy. It can be seen from the isolated Au_{14} density of states (DOS) spectrum in Fig. 4(a) that Au_{14} has a 1.8 eV HOMO-LUMO gap originating from its closed-shell electronic configuration. Upon interacting with nanotubes in the junction, these eigenstates broaden into resonances and shift to higher energies owing to an electron transfer from Au_{14} to the nanotubes, as shown in Fig. 4(b). An important effect of this energy shift is to bring the topmost occupied Au_{14} resonances closer to E_F, making them the dominant factor in determining low-bias electron transport. It is also clear from the PDOS plot that most of the topmost occupied Au_{14} resonances do not mix and this is partly due to the fact that interaction with the junction nanotubes preserves symmetries of the Au nanoparticle, thus forbidding nanoparticle eigenstates of different symmetries from mixing.

The isolated Au_{13} DOS and Au_{13} eigenstate PDOS share many similarities with corresponding quantities for the Au_{14} nanoparticle. The Au_{13} eigenstates broaden into resonances upon interacting with the nanotube junction and most resonances retain their eigenstate character owing to symmetry reasons mentioned earlier. But an important difference is that

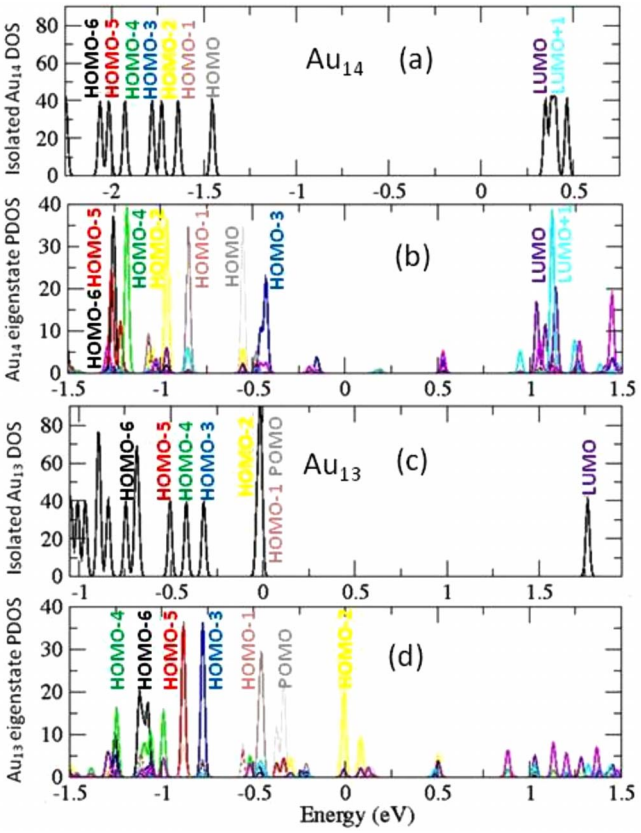

FIG. 4. (Color online) DOS of isolated (a) Au_{14} and (c) Au_{13} nanoparticles and the Au nanoparticle eigenstate PDOS for (b) Au_{14}- and (d) Au_{13}-decorated nanotube junctions. Colors in PDOS plots indicate nanoparticle eigenstates being projected on.

the Au_{13} nanoparticle has an odd number of electrons, resulting in a partially occupied molecular orbital (POMO) pinned to the chemical potential in the Au_{13} nanoparticle DOS and a HOMO-2 resonance pinned to the Fermi level E_F in the Au_{13} eigenstate PDOS. The presence of a resonance at E_F dramatically increases the conductance and low-bias current in Au_{13}-decorated nanotube junctions, leading to qualitatively different conduction properties from corresponding junctions bridged by Au_{14}.

Let us now investigate the topmost occupied Au nanoparticle eigenstates in more detail as they play an important role in determining electron transport close to E_F. As can be seen in Fig. 5(c), the Au_{14} nanoparticle possesses reflection symmetry about the σ_x and σ_y planes that are normal to the x and y axes, respectively. An inspection of the Au_{14} eigenstate wave function shows that the HOMO-1 eigenstate is odd about σ_x and even about σ_y, the HOMO-3 eigenstate even about σ_x and odd about σ_y, and the HOMO and HOMO-2 eigenstates even about both σ_x and σ_y. From Fig. 3(a), we find that the nanotube π and π^* bands are even and odd about the σ_x plane, respectively. Thus, we expect the HOMO-1 eigenstate to couple to the π^* band and the HOMO, HOMO-2, and HOMO-3 eigenstates to couple to the π band, consistent with the occurrence of band splitting in the junction band structure of Fig. 5(a). It is also clear from the band structure that only one of the two degenerate nanotube bands interacts with each Au_{14} eigenstate, the se-

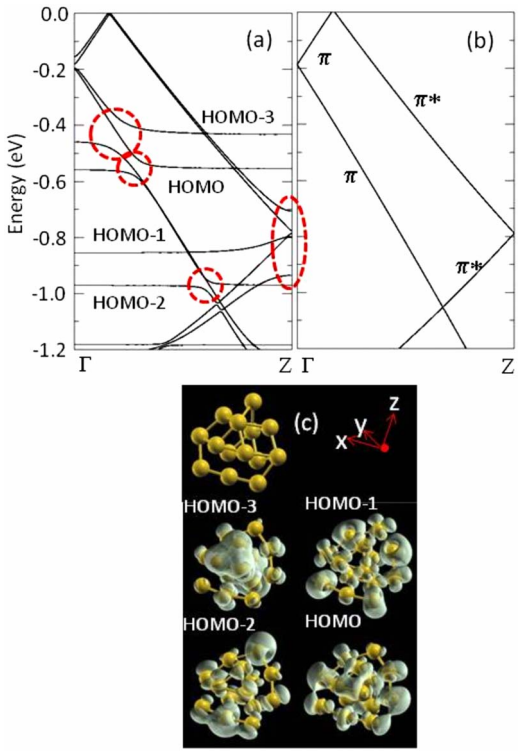

FIG. 5. (Color online) Band structure along nanotube axis direction for (a) Au_{14}-decorated nanotube junction and (b) bare nanotube junction. (c) Wave function density $|\phi_i|^2$ isosurfaces of topmost occupied Au_{14} eigenstates.

lection rule being that the eigenstate and nanotube band has to have similar reflection symmetries about the σ_y plane. The π^* band is known to be more delocalized than the π band owing to its more antibonding nature and this leads to an enhancement of the interaction between the nanotube and the HOMO-1 eigenstate, evidenced by the large HOMO-1-induced π^*-band splitting at $E \approx -0.85$ eV in Fig. 5(a). Also, the fact that the HOMO-3 has odd symmetry about σ_y means that its wave function density is localized away from the nanoparticle center and concentrated on Au nanoparticle faces adjacent to the junction nanotubes as shown in Fig. 5(c), giving rise to an increased nanotube–HOMO-3 interaction and a large band splitting at $E \approx -0.40$ eV. A similar analysis performed on Au_{13}-decorated nanotube junctions show that the above symmetry arguments apply equally well for the Au_{13} case. The Au_{13} POMO eigenstate interacts strongly with the nanotube as it is odd about σ_x and couples to the more delocalized nanotube π^* band, while the HOMO-2 eigenstate interacts strongly with the nanotube as it is odd about the σ_y plane and has wave function density localized on Au atoms adjacent to the junction nanotubes.

We can calculate the transmission spectrum and I-V characteristics using the scattering states formalism outlined earlier in the paper. To construct the geometry for these calculations, we take a relaxed nanotube structure and cap one end of it with half a C_{60} fullerene. The nanotube cap is then fully relaxed and two of these capped nanotubes are placed adjacent to an Au nanoparticle so that the nanoparticle coordinates and its position relative to the nanotubes are identical

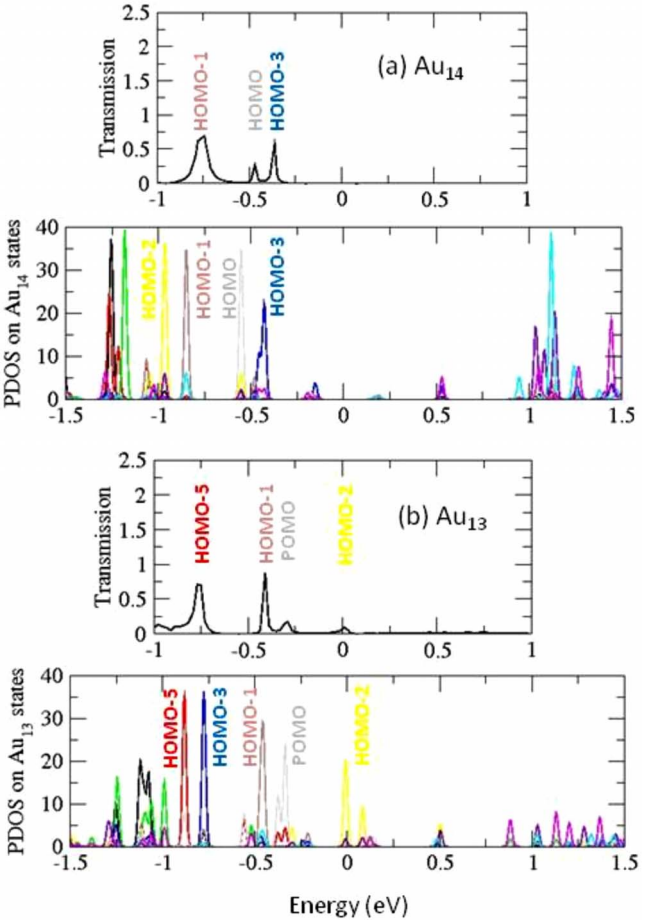

FIG. 6. (Color online) Transmission spectrum and Au nanoparticle eigenstate PDOS for (a) Au_{14}- and (b) Au_{13}-decorated nanotube junctions.

to that from the supercell calculation, as shown in Fig. 3(b). The lead unit cell is 3 nanotube unit cells long and several nanotube unit cells are included as a buffer between the leads and the Au nanoparticle.

It can be seen from Fig. 6 that each peak in the zero-bias transmission spectra originates from an Au nanoparticle resonance, giving clear indication of a resonant tunneling conduction mechanism. Owing to the presence of the HOMO-LUMO gap in Au_{14}, there is little transmission near the Fermi level E_F and a negligible conductance of 2×10^{-4} G_0 for Au_{14}-decorated nanotube junctions, as shown in Fig. 6(a). This can be contrasted with transmission across Au_{13}-decorated nanotube junctions in Fig. 6(b), where partially filled Au_{13} resonances ensure the presence of transmission peaks pinned to E_F and an appreciable conductance value of 0.09 G_0. This even-odd alternation in conductance values can be generalized to all Au nanoparticles with dimensions small enough to possess a sizable HOMO-LUMO gap.

It is reasonable to assume that the height and width of transmission peaks increase with the coupling strength between Au eigenstates and junction nanotubes. This is clearly the case for Au_{14}-decorated nanotube junctions, as can be seen by comparing the heights of transmission peaks in Fig. 6(a) to the sizes of band splitting in Fig. 5(a). However, this

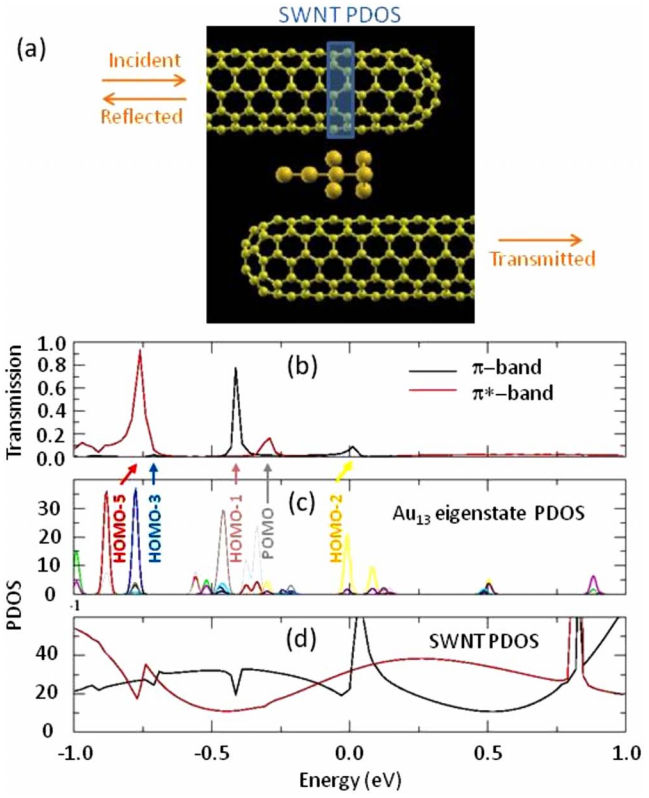

FIG. 7. (Color online) (a) Region of projection for SWNT PDOS indicated in shaded blue box. (b) Channel-resolved transmission spectrum. (c) PDOS on the Au_{13} eigenstates. (d) Nanotube PDOS [as defined in (a)] of π (black) and π^* (red) bands for the Au_{13}-decorated nanotube junction.

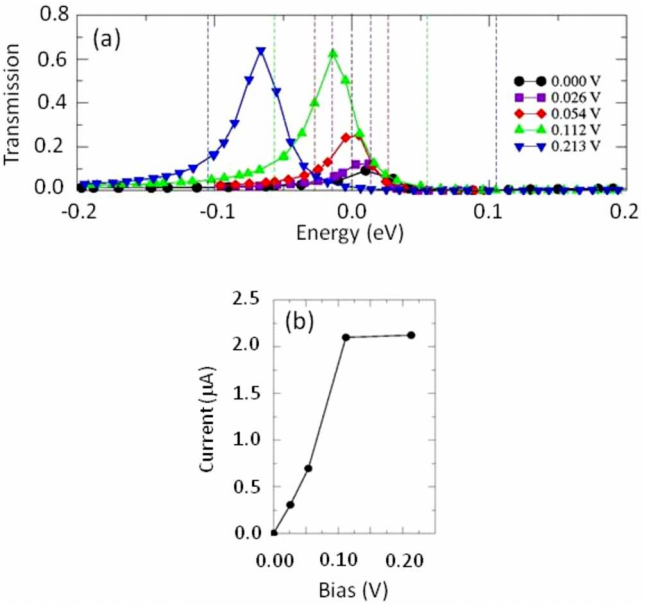

FIG. 8. (Color online) (a) Transmission spectra at various bias voltages and the (b) *I-V* characteristic of an Au_{13}-decorated nanotube junction.

expectation is not realized for Au_{13}-decorated nanotube junctions as it was found in the previous section that the Au_{13} POMO and HOMO-2 interact more strongly with the junction nanotubes than the HOMO-1 eigenstate, but the sizes of transmission peaks in Fig. 6(b) seem to suggest the opposite. Upon further inspection, these seemingly conflicting observations can be resolved by taking the effect of interference between incident and reflected electron waves into consideration.

To understand this interference effect and its impact on electron transport, we have plotted in Fig. 7(d) the PDOS on a segment of the nanotube closest to Au_{13}, as indicated in the blue box of Fig. 7(a). In an isolated armchair carbon nanotube, the density of states around E_F should be a constant owing to the linear dispersion of the π and π^* bands. However, we see bump and dips in the nanotube PDOS of Fig. 7(d) originating from the presence of Au_{13} resonances. But more interestingly, we also observe a gradual oscillation in the nanotube PDOS originating from the interference between incident and reflected electron waves bouncing off the end of the nanotube. This interference leads to the formation of standing waves that terminate close to the end of the nanotube and the PDOS on the nanotube close to Au_{13} could be high or low depending on the wavelength (or k vector/energy) of the incident electrons, as illustrated in Fig. 7(d).

From our earlier discussion on symmetries of the Au_{13} eigenstates, we know that of the top four partially/fully occupied eigenstates, only the POMO interacts with the π^* band while the HOMO-3, HOMO-2, and HOMO-1 states couple to the π band. It can be easily seen by comparing the Au_{13} eigenstate PDOS [in Fig. 7(c)] and the nanotube PDOS [in Fig. 7(d)] that the HOMO-2 resonance is aligned to a trough of the π-band PDOS. The absence of wave function density on the nanotube offsets the large hopping matrix element between this resonance and states of the nanotube π band, giving rise to a relatively small transmission peak. Similar arguments can be applied to explain the weak transmission mediated by the Au_{13} POMO, which couples strongly to the π^* band. The opposite is true of the HOMO-1 resonance, where its alignment to a crest of the nanotube π-band PDOS offsets its small hopping matrix element to the nanotube π band to generate a large transmission peak. Of the four topmost occupied resonances, the HOMO-3 transmission peak is the smallest owing to its alignment to the nanotube π-band PDOS trough and a small coupling to the π-band states.

By inspecting the transmission spectra in Fig. 6(a), it is clear that the low-bias current in Au_{14}-decorated nanotube junctions is negligible owing to a lack of resonance peaks close to E_F. On the other hand, the Au_{13}-decorated nanotube junction has a HOMO-2 derived transmission peak centered in the bias window whose amplitude increases substantially as the bias voltage is increased, as shown in Fig. 8(a). The reason for this increase is clear by superimposing the nanotube PDOS in Fig. 7(d) onto the transmission spectra in Fig. 8(a), which shows the transmission peak moving away from the trough of the incident (higher chemical potential) SWNT π-band PDOS with increasing bias voltage. Since the current is obtained by integrating the transmission in the bias window, an increase in the transmission peak height translates into an increasing gradient in the *I-V* curve, as can be seen for low-bias voltages in Fig. 8(b). At sufficiently high bias

voltages, the entire transmission peak is within the bias window and the current plateaus.

IV. CONCLUSION

Motivated by recent experimental work in metal-nanoparticle-doped nanotube networks,[8–10] we have performed first-principles calculations on Au-nanoparticle-decorated nanotube junctions. Electron transport across these junctions was found to be mediated by resonant tunneling across the topmost occupied Au nanoparticle resonances and corresponding transmission amplitudes demonstrate a strong dependence on the orientation and symmetry of these resonances relative to the nanotube states. We find that only nanotube junctions bridged by odd-numbered Au nanoparticles show appreciable conductance owing to the fact that even-numbered Au nanoparticles have a HOMO-LUMO gap originating from their closed-shell electronic configuration. Conductance values obtained for odd-numbered Au nanoparticle junctions are at least 1 order of magnitude larger than typical values calculated for bare nanotube junctions,[25] consistent with experimental observations of conductance increase in doped nanotube networks. Additionally, the electron transport in nanotube junctions bridged near the nanotube end caps is modulated by effects resulting from the interference between incident and reflected electron waves in nanotubes.

ACKNOWLEDGMENTS

We would like to thank Rod Ruoff for numerous valuable discussions. This work has been supported in part by the National Science Foundation under Contract No. DMR-0551195 and the U.S. Department of Energy under Contracts No. DEFG02-06ER15760 and No. DE-FG02-06ER46286. Calculations were performed at the National Energy Research Scientific Computing Center (NERSC) and Texas Advanced Computing Center (TACC).

[1] V. Georgakilas, D. Gournis, V. Tzitzios, L. Pasquato, D. M. Guldi, and M. Prato, J. Mater. Chem. **17**, 2679 (2007).
[2] J. Kong, M. G. Chapline, and H. Dai, Adv. Mater. **13**, 1384 (2001).
[3] Q. Zhao, M. B. Nardelli, W. Lu, and J. Bernholc, Nano Lett. **5**, 847 (2005).
[4] H. S. Kim, H. Lee, K. S. Han, J. H. Kim, M. S. Song, M. S. Park, J. Y. Lee, and J. K. Kang, J. Phys. Chem. B **109**, 8983 (2005).
[5] E. Durgun, S. Ciraci, and T. Yildirim, Phys. Rev. B **77**, 085405 (2008).
[6] J. M. Planeix, N. Coustel, B. Coq, V. Brotons, P. S. Kumbhar, R. Dutartre, P. Geneste, P. Bernier, and P. M. Ajayan, J. Am. Chem. Soc. **116**, 7935 (1994).
[7] S. Ravindran, S. Chaudhary, B. Colburn, M. Ozkan, and C. S. Ozkan, Nano Lett. **3**, 447 (2003).
[8] B. S. Kong, D. H. Jung, S. K. Oh, C. S. Han, and H. T. Jung, J. Phys. Chem. C **111**, 8377 (2007).
[9] G. Lawson, F. Gonzaga, J. Huang, G. de Silveira, M. A. Brook, and A. Adronov, J. Mater. Chem. **18**, 1694 (2008).
[10] Y. C. Chen, R. J. Young, J. V. Macpherson, and N. R. Wilson, J. Phys. Chem. C **111**, 16167 (2007).
[11] E. S. Snow, J. P. Novak, P. M. Campbell, and D. Park, Appl. Phys. Lett. **82**, 2145 (2003).
[12] K. Bradley, J. P. Gabriel, and G. Gruner, Nano Lett. **3**, 1353 (2003).
[13] Z. Wu, Z. Chen, X. Du, J. M. Logan, J. Sippel, M. Nikolou, K. Kamaras, J. R. Reynolds, D. B. Tanner, A. F. Hebard, and A. G. Rinzler, Science **305**, 1273 (2004).
[14] J. M. Soler, E. Artacho, J. D. Gale, A. Garcia, J. Junquera, P. Ordejon, and D. Sanchez-Portal, J. Phys.: Condens. Matter **14**, 2745 (2002).
[15] E. Artacho, D. Sanchez-Portal, P. Ordejon, A. Garcia, and J. M. Soler, Phys. Status Solidi B **215**, 809 (1999).
[16] J. P. Perdew, K. Burke, and M. Ernzerhof, Phys. Rev. Lett. **77**, 3865 (1996).
[17] N. Troullier and J. L. Martins, Phys. Rev. B **43**, 1993 (1991).
[18] H. J. Choi, M. L. Cohen, and Steven G. Louie, Phys. Rev. B **76**, 155420 (2007).
[19] J. K. Tomfohr and O. F. Sankey, Phys. Rev. B **65**, 245105 (2002).
[20] S. Datta, *Electronic Transport in Mesoscopic Systems* (Cambridge University Press, Cambridge, England, 1995).
[21] X. B. Li, H. Y. Wang, X. D. Yang, Z. H. Zhu, and Y. J. Tang, J. Chem. Phys. **126**, 084505 (2007).
[22] H. Hakkinen, M. Moseler, and U. Landman, Phys. Rev. Lett. **89**, 033401 (2002).
[23] Y. Dong and M. Springborg, J. Phys. Chem. C **111**, 12528 (2007).
[24] J. Akola and H. Hakkinen, Phys. Rev. B **74**, 165404 (2006).
[25] A. Buldum and J. P. Lu, Phys. Rev. B **63**, 161403(R) (2001).